Surf zone surface retention on a rip-channeled beach

A. J. H. M. Reniers,[1,2] J. H. MacMahan,[3] E. B. Thornton,[3] T. P. Stanton,[3] M. Henriquez,[2] J. W. Brown,[4] J. A. Brown,[4,5] and E. Gallagher[6]

[1] The retention of floating matter within the surf zone on a rip-channeled beach is examined with a combination of detailed field observations obtained during the Rip Current Experiment and a three-dimensional (3-D) wave and flow model. The acoustic Doppler current profiler–observed hourly vertical cross-shore velocity structure variability over a period of 3 days with normally incident swell is well reproduced by the computations, although the strong vertical attenuation of the subsurface rip current velocities at the most offshore location outside the surf zone in 4 m water depth is not well predicted. Corresponding mean alongshore velocities are less well predicted with errors on the order of 10 cm/s for the most offshore sensors. Model calculations of very low frequency motions (VLFs) with $O(10)$ min timescales typically explain over 60% of the observed variability, both inside and outside of the surf zone. The model calculations also match the mean rip-current surface flow field inferred from GPS-equipped drifter trajectories. Seeding the surf zone with a large number of equally spaced virtual drifters, the computed instantaneous surface velocity fields are used to calculate the hourly drifter trajectories. Collecting the hourly drifter exits, good agreement with the observed surf zone retention is obtained provided that both Stokes drift and VLF motions are accounted for in the modeling of the computed drifter trajectories. Without Stokes drift, the estimated number of virtual drifter exits is $O(80)$%, almost an order of magnitude larger than the $O(20)$% of observed exits during the drifter deployments. Conversely, when excluding the VLF motions instead, the number of calculated drifter exits is less than 5%, thus significantly underestimating the number of observed exits.

1. Introduction

[2] The surf zone is an important conduit for the transport of sediment [e.g., *Komar*, 1976], pollutants [*Grant et al.*, 2005], and other suspended matter (diatoms, algae, bubbles, and larvae). In the case of obliquely incident waves, a longshore current develops transporting suspended matter in the down-wave direction. Under these conditions, field observations suggest that initially present suspended matter is mostly confined to the surf zone and the cross-shore exchange with the inner shelf is minimal [*Inman et al.*,

1971; *Johnson and Pattiaratchi*, 2004; *Clarke et al.*, 2007]. However, on beaches with persistent shore-normal wave conditions the longshore current is mostly absent and instead rip currents develop. The prevailing idea in this case is that suspended matter is transported onshore by the breaking waves over the shallow shoals feeding into a rip channel where offshore directed rip currents subsequently deposit the material well outside the surf zone [*Inman and Brush*, 1973]. Starting with an initial concentration of suspended matter, it would therefore be expected that the surf zone purges itself much more rapidly in the case of persistent shore-normal waves compared with the case of a steady longshore current.

[3] There are several processes that contribute to the transport of suspended and floating matter within the nearshore. The advection and dispersion associated with the mean flow mentioned earlier is accompanied by transport because of vortical motions at shorter time scales, $O(10)$ min, such as shear instabilities [e.g., *Dodd et al.*, 2000; *Özkan-Haller and Kirby*, 1999; *Haller and Dalrymple*, 2001] and wave group induced very low frequency motions (VLFs) [*MacMahan et al.*, 2004; *Reniers et al.*, 2007]. Both infragravity waves, at the timescale of wave groups $O(50)$ s, and incident short waves with $O(10)$ s wave

[1]Applied Marine Physics Department, RSMAS, University of Miami, Miami, Florida, USA.
[2]Department of Hydraulic Engineering, Delft University of Technology, Delft, Netherlands.
[3]Department of Oceanography, Naval Postgraduate School, Monterey, California, USA.
[4]Center for Applied Coastal Research, University of Delaware, Newark, Delaware, USA.
[5]Now at Department of Oceanography, Naval Postgraduate School, Monterey, California, USA.
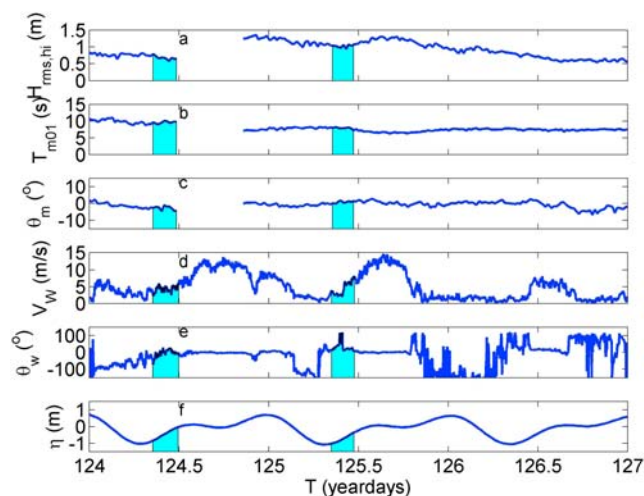[6]Department of Biology, Franklin and Marshall College, Lancaster, Pennsylvania, USA.

Figure 1. Environmental conditions used in the model-RCEX data comparisons. (a) Root mean square incident wave height, (b) mean wave period and (c) mean wave direction at 12.8 m water depth. (d) Wind speed and (e) wind direction at Del Monte (2 km south of the field site). (f) Tidal elevation at NOAA tidal station in Monterey harbor (4 km south of the experimental site). Time of drifter deployments on yeardays 124 and 125 indicated in cyan.

periods, can contribute to the transport if the concentration of suspended matter is a nonlinear function of the orbital velocity and/or fall velocity, for example, sand stirred up from the bed by the wave-induced shear stress. In the case of infragravity waves, this leads to predominantly offshore transport, whereas nonlinear short waves generally result in net onshore transport [*Roelvink and Stive*, 1989]. In addition, short wave–averaged orbital fluid particle paths of finite amplitude short waves are not fully closed resulting in a net drift in the down-wave direction, known as Stokes drift [*Stokes*, 1847; *Phillips*, 1977]. Stokes drift has its maximum at the surface and is therefore expected to be important for the transport of surface floating material [*Monismith and Fong*, 2004]. Finally, mixing by wave breaking induced turbulence strongly contributes to the local diffusion of suspended matter [*Battjes*, 1975; *Feddersen*, 2007; *Brown et al.*, 2008].

[4] To examine the retention of surf zone material on a rip-channeled beach a combination of detailed measurements obtained during the 2007 Rip Current Experiment (RCEX) (J. MacMahan et al., Mean Lagrangian observations on open coast rip-channeled beaches, submitted to *Marine Geology*, 2009) and a 3-D wave and flow model is used (Delft3D) [*Lesser et al.*, 2004]. The field measurements are obtained with both GPS-equipped surface drifters and in situ pressure and colocated current velocity meters. Given the complexity of following a large number of individual suspended particles within the surf zone, the behavior of the surface drifters is examined instead. The drifters are designed to mitigate the effects associated with wave-breaking-induced surface rollers and were shown to closely follow the dispersion of a dye patch, thus corresponding to a Lagrangian measurement including Stokes drift [*MacMahan et al.*, 2008]. Note that surface floating material is not subject to fall velocity and, as such,

is minimally affected by infragravity waves [*Spydell et al.*, 2007] and skewed incident waves. Given the expected presence of vertical variation within the rip current velocity field [*MacMahan et al.*, 2005], it is important to utilize a 3-D flow model to calculate the surface flow velocities.

[5] Three-dimensional modeling of the nearshore flow field is often restricted to cases where the alongshore variation is absent, for example, in a wave flume, essentially resulting in 2DV computations [*Walstra et al.*, 2000; *Nobuoka et al.*, 2004]. Alternatively the model equations are solved in a quasi-3-D (Q3D) approach, i.e., solving for the depth-averaged shallow water equations and applying a vertical flow model a posteriori [*van Dongeren et al.*, 2003; *Haas et al.*, 2003]. A recent application of a Q3D [*Putrevu and Svendsen*, 1999] and full 3-D [*Mellor*, 2003] model description to calculate mean nearshore flows gave comparable results both showing good agreement compared with laboratory observations [*Haas and Warner*, 2009]. Here full 3-D model computations are used to predict the 3-D structure of the rip-current circulation present during RCEX. The flow model is driven by wave momentum and pressure gradients varying on the wave groupscale [*Reniers et al.*, 2004, 2006, 2007], thus resolving the mean, VLF, and infragravity motions. Solving for the Generalized Lagrangian Mean (GLM) velocities accounts for the wave-induced Stokes drift [*Andrews and McIntyre*, 1978; *Groeneweg and Klopman*, 1998; *Walstra et al.*, 2000].

[6] The model is verified by comparing with the RCEX observations. This includes the mean surface flow circulation obtained with the surface drifters, the vertical structure of the nearshore flow, VLF motions, and the wave transformation within the surf zone. Next the model is used to examine the fate and retention of surface floating material, represented by surf zone drifters, during persistent normally incident swell with specific attention for the effects related to Stokes drift and rip-related VLFs.

2. Observations

[7] During the Rip Current Experiment (RCEX), in the spring of 2007 a combination of fixed in situ instruments and surface drifter deployments were used to map rip current circulations (MacMahan et al., submitted manuscript, 2009). The environmental conditions chosen for the 3 days of model-data comparisons discussed below correspond to moderate, normally incident wave conditions (Figure 1) that includes two drifter deployments. On yearday 124 the root mean square incident wave height, H_{rms}, was 0.7 m, the mean wave period, T_{m01}, was 10 s, and the tidal elevation with respect to mean sea level (MSL), η, ranged from -0.8 m at the start (around 9 am) to 0 m at the end of the deployment (around 12 pm local time) (Figure 1). The tidal range during the drifter deployment on yearday 125 was similar, but with a more energetic H_{rms} of 1.0 m and a T_{m01} of 8 s.

[8] Bathymetric surveys were performed using a kinematic, global positioning system (KGPS) mounted on a sonar-equipped personal watercraft (PWC) [*MacMahan*, 2001]. At high tides and low wave energy conditions, the PWC traversed from offshore to the outer edge of the transverse bars and within the rip channels (Figure 2). At low tides, the transverse bars and feeder channels were
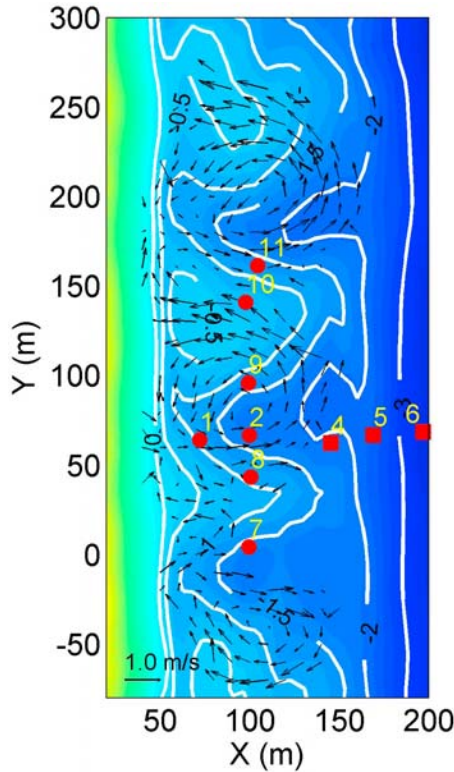
Figure 2. Surface velocity vectors (velocity scale in lower left corner) for yearday 124 obtained from the surface drifters averaged over the duration of the drifter deployment. Position of instruments indicated by the red circles (PDEMS) and squares (ADCPs). Bathymetry surveyed on yearday 121 with bottom contours (white lines) in meters with respect to MSL given as a reference.

surveyed by a walking person carrying the KGPS housed in a watertight backpack. The beachface and foredune were surveyed with the KGPS mounted on an all-terrain vehicle. The bathymetry surveyed on yearday 121, used in the model calculations discussed below, shows that the alongshore separation of the quasi-steady rip channels is $O(125)$ m and the channels extend approximately $O(125)$ m offshore relative to the shore line (Figure 2).

[9] The GPS-derived drifter locations sampled at 0.5 Hz for the approximate 3 h duration of the drifter deployment are used to infer the mean surface flow velocity field (Figure 2). Given the fact that the drifters provide a Lagrangian measurement, the estimated velocities include Stokes drift. In addition to the drifter deployments, a combined alongshore and cross-shore array of colocated pressure and current velocity meters (either digital electromagnetic flowmeters (PDEMs) or acoustic Doppler current profilers (ADCPs)) were deployed (Figure 2). The PDEMs and ADCPs were continuously sampled at 15 Hz and 1 Hz, respectively. More details about the drifter deployments are given by MacMahan et al. (submitted manuscript, 2009).

3. Modeling Approach

[10] The wave and flow modeling is similar to the method by *Reniers et al.* [2004, 2006], in which the precomputed

wave refraction obtained with SWAN [*Booij et al.*, 1999] is used to solve for the wave and roller energy balance on the wave group timescale (see Appendix A). The SWAN wave refraction computations include both bathymetric and depth-averaged current refraction at the VLF timescale. The offshore boundary of the model domain starts at 12.8 m depth. The alongshore domain follows the coast for 1 km, where the lateral boundaries are located 600 m upcoast and 400 m downcoast of the cross-shore array. A cross-shore varying grid is used to compute the wave group transformation from offshore to the shoreline with the smallest grid spacing around the 1 m depth contour, where wave breaking is generally the most intense. The vertical grid spacing is with 10 percent increments of the total water depth (including the tidal elevation, mean setdown/setup, and infragravity elevations). The offshore boundary conditions for the wave energy balance are obtained from the hourly frequency-directional wave spectra calculated from the offshore ADCP using a single summation random phase model [*van Dongeren et al.*, 2003]. The spatial and temporal variations in the wave and roller energy are used to calculate the wave forcing. This wave forcing is introduced into the nonlinear shallow water flow model to calculate the wave group induced flow motions. The time step in the calculations is set at 3 s, thereby resolving wave group motions of 25 s and longer. Model coefficients for bottom friction, n (Manning coefficient), wave breaking, γ, and roller dissipation, β, are set at 0.02, 0.45, and 0.1, respectively, established from the calibrations by *Reniers et al.* [2006].

[11] In the following, a brief synopsis of the 3-D GLM flow model equations is presented. A detailed description of the 3-D flow modeling is given by *Lesser et al.* [2004, and references therein]. The 3-D flow field is calculated with the nonlinear shallow water equations. The corresponding cross-shore momentum equation is given by

$$\frac{\partial u}{\partial t} + u\frac{\partial u}{\partial x} + v\frac{\partial u}{\partial y} + w\frac{\partial u}{\partial z} - fv = -g\frac{\partial \zeta}{\partial x} + F_B^x + H_x$$
$$+ \frac{\partial}{\partial z}\left(\nu_v\frac{\partial u}{\partial z}\right) \qquad (1)$$

where u represents the cross-shore GLM velocity (x direction), v is the alongshore GLM velocity (y direction), w is the vertical velocity (z direction), ζ is the instantaneous surface elevation, f is the Coriolis parameter, F_B^x is the wave forcing (where the superscript denotes direction), H_x are the cross-shore turbulent mixing terms, ν_v is the vertical turbulent eddy viscosity, and g is the gravitational acceleration. A similar expression is used for the alongshore momentum equation. The Eulerian velocities are calculated by subtracting the Stokes drift, $\mathbf{u^s}$, from the GLM flow velocities [*Andrews and McIntyre*, 1978]:

$$\mathbf{u}^e = \mathbf{u} - \mathbf{u^s} \qquad (2)$$

where $\mathbf{u}$ represents the GLM velocity vector (u, v) and the Stokes drift is a combination of the depth-varying wave-
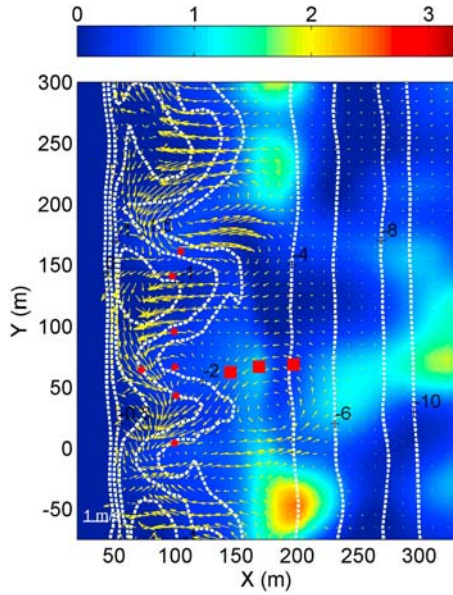
Figure 3. Snapshot of computed wave energy (denoted by colors) in KJ/m^2 and corresponding GLM surface velocity (velocity scale in lower left corner) for yearday 124 at 11.00 h (equivalent to yearday 124.46). Bottom contours (white lines) in meters given as a reference.

related Stokes drift [*Phillips*, 1977] and a roller contribution [*Svendsen*, 1984] given by

$$\mathbf{u}^s = \frac{\omega k_w H^2 \cos h(2k_w(h+z))}{8 \sin h^2(k_w h)} \frac{\mathbf{k_w}}{k_w} + \mathbf{u^r} \qquad (3)$$

where $\mathbf{u^r}$ represents the roller-related Stokes drift (equation (A3) in Appendix A), h represents the total water depth, and $\mathbf{k_w}$ represents the wave number vector of the incident waves with magnitude k_w. The wave vector field is obtained from the SWAN precomputed wave refraction, and the instantaneous wave height, H, is obtained from the wave group energy balance (see equation (6) below). A k-ϵ model is used to calculate ν_v, where the wave breaking induced turbulence is introduced as a source term linearly distributed from minus $H_{rms,hi}$ to the water surface elevation (twice the distance used by *Walstra et al.* [2000]).

[12] The wave forcing, **F**, is implemented by considering both the rotational and irrotational wave motions [*Dingemans et al.*, 1987]. The rotational contribution is represented by a shear stress at the sea surface, $\boldsymbol{\tau}_s$, related to wave breaking [*Deigaard*, 1993]:

$$\boldsymbol{\tau}_s = \frac{D_R}{c} \frac{\mathbf{k_w}}{k_w} \qquad (4)$$

where D_R represents the roller energy dissipation (equation (A2) in Appendix A) and c is the wave phase speed. The irrotational part is obtained by subtracting the rotational contribution from the total wave forcing represented by the spatial gradients in radiation stress S_{ij}:

$$F_B^x = \frac{1}{\rho h}\left(\frac{\partial S_{xx}}{\partial x} + \frac{\partial S_{xy}}{\partial y}\right) - \tau_s^x \qquad (5)$$

and is applied as a depth-invariant wave force in equation (1). The total surface stress is given by the combined surface wave and wind stress, where the latter is computed with a quadratic friction law using the locally measured wind speed (Figure 1). Details on the boundary conditions and numerical solution procedures are given by *Lesser et al.* [2004] and *Walstra et al.* [2000].

4. Wave Transformation

[13] The wave and flow response at the wave group timescale is calculated for 3 days from yearday 124 to yearday 127, taking into account the temporal changes in the offshore wave conditions, wind forcing, and concurrent tidal elevation (Figure 1). The model results for the duration of the drifter deployment on yearday 124 are discussed next. A snapshot of the computed wave energy, E_w, for yearday 124 at 11.00 hr shows spatial variation in both the alongshore and cross-shore directions (Figure 3). The alongshore variation outside the surf zone, $x > 170$ m, is associated with the directional spreading of the short waves [*Reniers et al.*, 2004]. Within the surf zone, the effect of the alongshore variation in the rip-channeled bathymetry becomes dominant with wave breaking on the shallow shoals and continuous wave propagation within the deeper rip channels. The corresponding snapshot of the instantaneous surface velocities show that wave breaking on the shoals and concurrent shear stresses result in an onshore flow (Figure 3). As this flow approaches the waterline, it is laterally diverted thereby feeding the offshore directed rip currents resulting in strong vortical circulations coupled with the underlying morphology (Figure 3). The offshore extent of the rip currents at this time is mostly limited to the outer edge of the surf zone, although occasionally they extend well beyond the surf zone, as observed around $y = 0$, where a VLF eddy has propagated offshore.

[14] The cross-shore transformation of H_{rms} obtained from the balance of wave energy, E_w:

$$H_{rms}(\mathbf{x}, t_i) = \sqrt{\frac{1}{\tau_{hour}} \int_{t_i}^{t_i+\tau_{hour}} \left[\frac{8E_w(\mathbf{x}, t)}{\rho g}\right] dt} \qquad (6)$$

is used to assess the wave forcing, where τ_{hour} represents a duration of 1 h and i refers to the hourly interval. A quantitative comparison of the measurements and computations is expressed as model skill [*Gallagher et al.*, 1998]:

$$skill = 1 - \frac{\sum_{i=1}^{i=N} \sqrt{(Q_{c,i} - Q_{m,i})^2}}{\sum \sqrt{Q_{m,i}^2}} \qquad (7)$$

where the subscripts c and m refer to computed and measured quantities, which are evaluated at all observed instances i. Computed H_{rms} values are compared with observations at the cross-shore array locations by replacing Q with H_{rms} in equation (7) resulting in a array-averaged skill of $O(0.8)$ similar to previous comparisons at this site [*Reniers et al.*, 2006] using the modeling approach outlined above. Note that a correct wave transformation prediction is essential to the computed flow response as it affects the wave forcing (equations (4) and (5)), Stokes drift
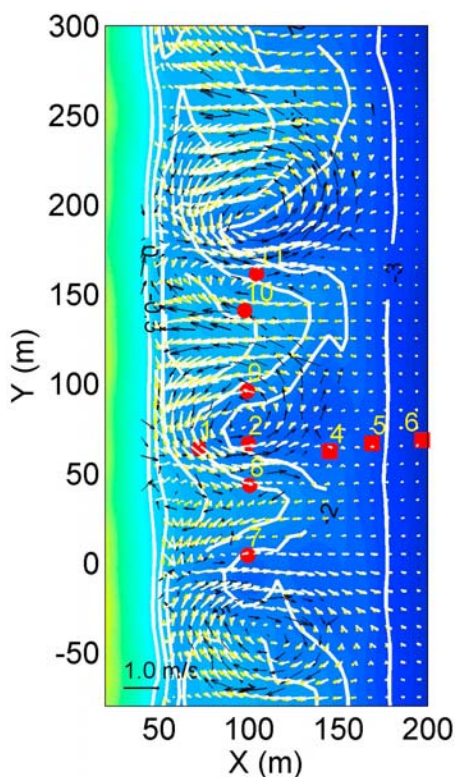
Figure 4. Mean (3 h) surface velocity vectors (velocity scale in lower left corner) for drifter deployment on yearday 124 obtained from the surface drifters (black arrows), Eulerian model computations (white arrows), and GLM computations (yellow arrows). Position of instruments indicated by the red circles (PDEMS) and squares (ADCPs). Bathymetry with bottom contours (white lines) in meters given as a reference.

(equation (3)), the turbulent eddy viscosity, and associated mixing terms (equation (1)).

5. Surface Flows

[15] Averaging the wave group resolving surface velocities over the 3 h duration of the drifter deployment on yearday 124 yields the mean surface velocity field that is compared with the GPS drifter-inferred mean velocities (Figure 4). The computations show similar flow circulations as the observations with onshore velocities over the shallow shoals feeding into the rip currents. Details on the flow divergence and convergence of the asymmetric flow circulations within the surf zone are also well represented (Figure 5 (left)). The offshore extent of the rips are limited because of the fact that the offshore flow quickly diverges resulting in mean vortical circulations. Note that the GLM and Eulerian mean flow circulations are significantly less at the outer edge of the surf zone ($X \sim 170$ m) than in the instantaneous flow field depicted in Figure 3. This illustrates the potential transport of surface material leaving the surf zone by means of VLF motions, where pulsations not captured by the mean flow are important for transport. The model skill, equation (7), for the mean surface velocity magnitude and direction is 0.6 and 0.65. In view of the potential effects of small bathymetric errors [Plant et al., 2009] this is considered a good match. The GLM and Eulerian mean flow velocities are very similar with near identical skill (compare Figures 5 (left) and 5 (middle)). However, a detailed look at the flow velocities at the outer surf zone shows that the Eulerian flow field generally has stronger offshore directed velocities (Figure 5 (right)). The alongshore velocities are only moderately affected, and as a result, the GLM velocities exhibit a stronger rotation (i.e., smaller radius) and at times opposite flow directions compared with the Eulerian velocities. Similar results are
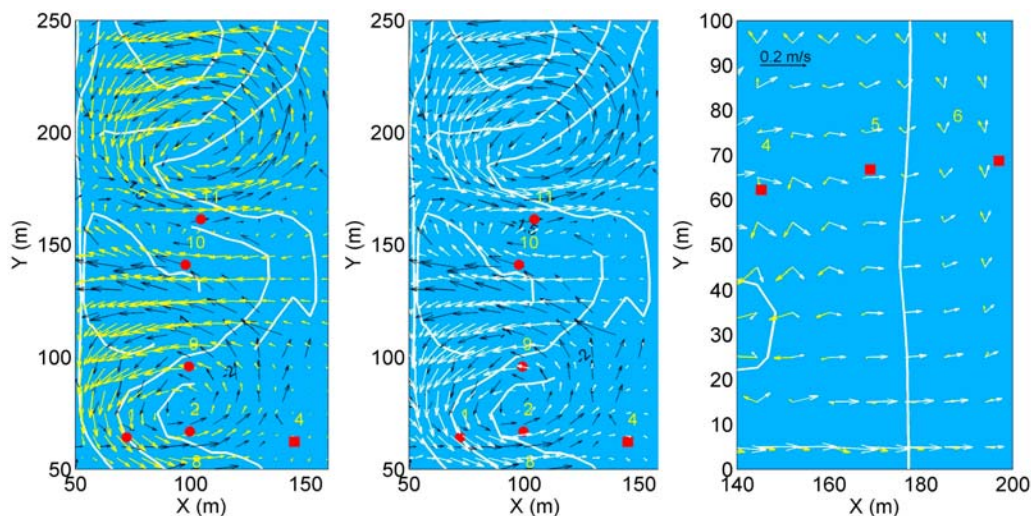

Figure 5. Details of Figure 4 with mean GLM (yellow arrows), mean Eulerian (white arrows), and GPS drifter-inferred (black arrows) surface velocity vectors. (left) Mean GLM surface circulation within the surf zone (velocity scale similar to Figure 4). (middle) Mean Eulerian surface circulation within the surf zone (velocity scale similar to Figure 4). (right) Mean surface circulation at the outer surf zone and beyond (velocity scale in upper left corner). Position of ADCPs (red squares) and PDEMS (circles) and bottom contours (white lines) in meters given as a reference.
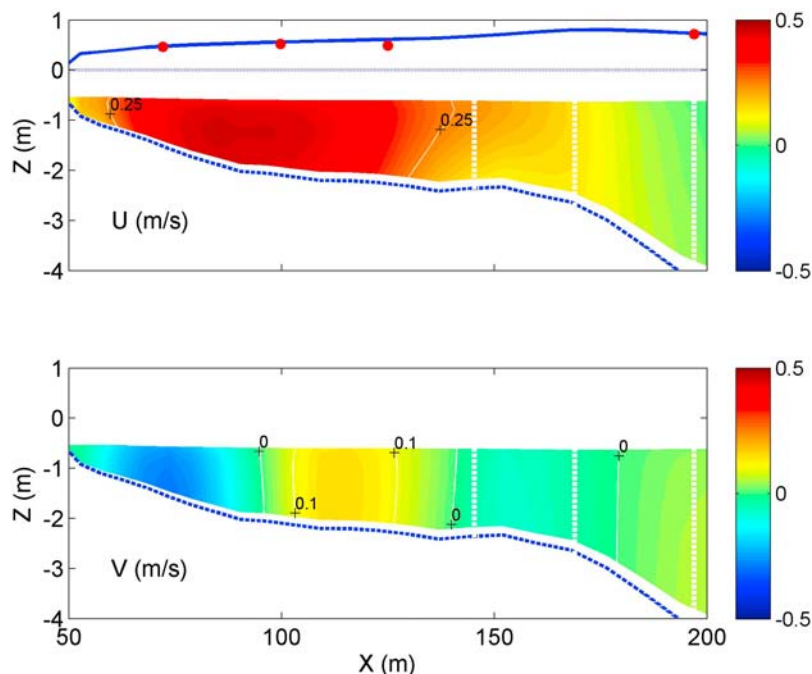
Figure 6. Computed hourly mean (top) cross-shore and (bottom) alongshore Eulerian flow velocity (positive offshore and downcoast) at cross-shore transect for yearday 124.46. Locations of ADCP4 (x = 145 m), ADCP5 (x = 169 m), and ADCP6 (x = 197 m) indicated by the white vertical dashed lines. Measured (red dots) and computed (solid line) H_{rms} given. MSL (dotted line) given as a reference.

obtained for the drifter deployment on yearday 125 (not shown).

6. Vertical Structure

[16] The computed vertical distribution of the horizontal velocities at the 1 h mean timescale are compared with the ADCP observations. A typical example of the computed vertical structure of a mean rip current flow shows that the strongest offshore velocities are located well within the surf zone, x < 125 m (Figure 6), with nearly depth-uniform offshore directed velocities of $O(0.5)$ m/s. At the outer surf zone (x > 125 m), maximum velocities occur just beneath the mean water surface with smaller velocities below resulting in significant vertical structure (similar to the results of *Haas and Warner* [2009]). The corresponding alongshore velocities are significantly smaller ($O(0.1)$ m/s) with little vertical variation both inside and outside the surf zone.

[17] Comparison with the observed hourly mean velocities shows qualitative agreement, both at ADCP4 (Figure 7) and ADCP6 (Figure 8). At ADCP4, both observed and modeled cross-shore velocities display strong temporal variation over a 3 day period with maximum offshore directed velocities coinciding with low water (Figure 7 (left)). The increased $H_{rms,hi}$ from the end of yearday 124 until the beginning of yearday 126 (Figure 1) is reflected in the increased rip current velocities for higher tidal elevations. Computed longshore current velocities generally underestimate the observed velocities, but they do exhibit similar but significantly weaker temporal variation (right

panels of Figure 7). Further offshore at ADCP6, the observations show a clear dominance of the cross-shore surface flow compared with the interior flow, which is not matched by the computations (Figure 8 (left)). This suggests that the combined wave forcing and turbulent eddy viscosity distribution (equation (1)) is not complete. Aside from the vertical distribution, the cross-shore velocity magnitude and temporal variability are well represented and do show the strong decay of the rip current flow velocity with increasing distance from the shore (compare cross-shore velocities in Figures 7 and 8). Model skill for the cross-shore near-surface flow is 0.56, 0.46, and 0.47 with corresponding RMS errors of 16 cm/s, 6 cm/s, and 4 cm/s for ADCPs 4, 5, and 6. The longshore current velocity at ADCP6 has negligible vertical variation in both model predictions and observations, with model predictions generally being significantly smaller than the observations (Figure 8 (right)). Model skill for the alongshore mean flow is 0.23, 0.16, and 0.1 with corresponding errors of 9 cm/s, 13 cm/s, and 12 cm/s for ADCPs 4, 5, and 6. The presence of stronger alongshore velocities with increasing depth, compare ACDP6 with ACDP4, suggests an ambient flow which is not included in the modeling.

[18] In summary, the mean surf zone surface flow is well represented by the model with similar spatial flow patterns as obtained from the drifter observations explaining 60% of the observed variability. Surface flow divergence and convergence as well as the offshore extent are well matched by both the GLM and Eulerian velocities. The Eulerian flows show a fair match compared with the ADCP measurements. This holds for cross-shore velocity magnitude, temporal
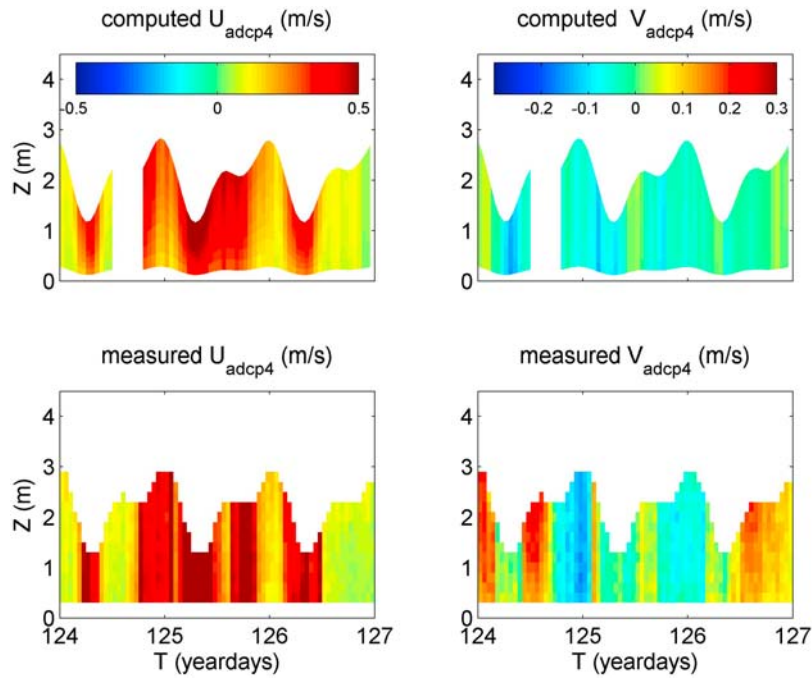
Figure 7. Hourly mean flow velocity at ADCP4. (top) Computed (left) cross-shore and (right) alongshore Eulerian velocity (positive offshore and downcoast). (bottom) Similar for observed velocities.

variation and offshore attenuation of the rip current flow velocities. The vertical structure of the Eulerian mean is less well represented, especially further offshore where the strong vertical attenuation of the observed subsurface cross-shore flow velocity is not present in the model results (Figure 8 (left)). Alongshore current velocities at the offshore ADCPs are not well predicted and may be related to

small ambient forcing with RMS errors on the order of 10 cm/s.

7. VLF Modeling

[19] The model-calculated and measured near-surface Eulerian velocities for the duration of the drifter experiment
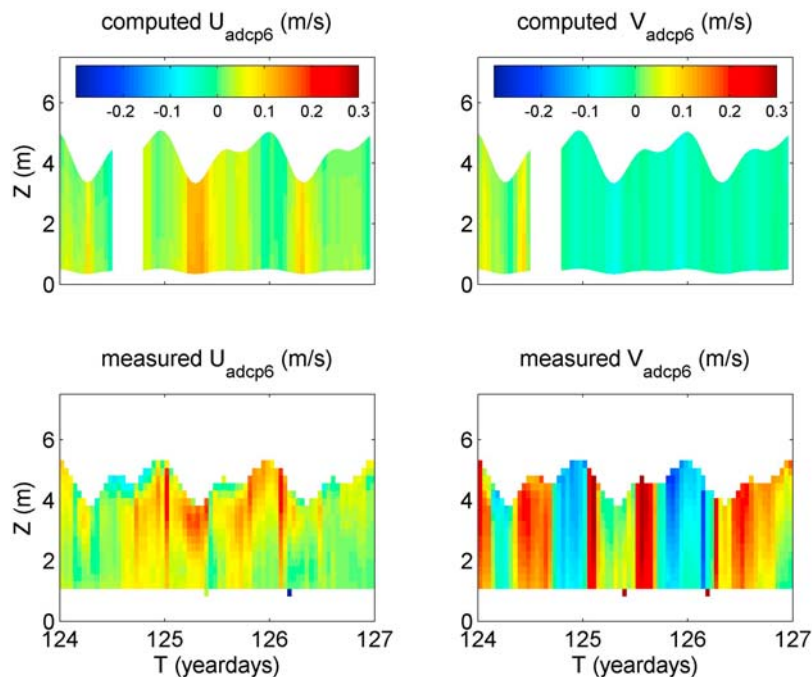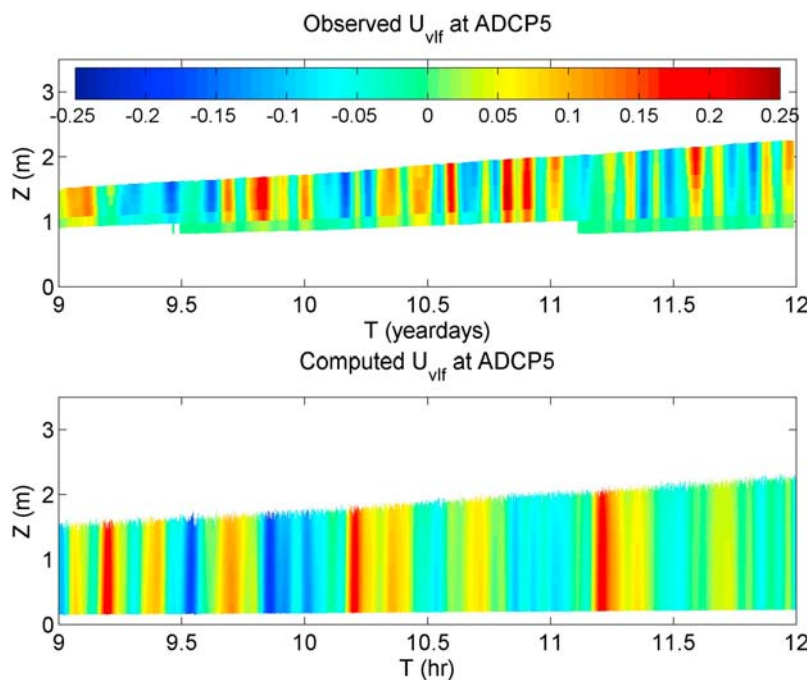

Figure 8. Hourly mean flow velocity at ADCP6. (top) Computed (left) cross-shore and (right) alongshore Eulerian velocity (positive offshore and downcoast). (bottom) Similar for observed velocities.

Figure 9. VLF conditions during drifter deployment on yearday 124. (top) Observed VLF cross-shore velocity at ADCP5. (bottom) Concurrent model prediction at ADCP5.

on yearday 124 are linearly detrended and low-pass filtered with a frequency cutoff of 0.004 Hz. The 0.004 Hz cutoff is based on earlier observations and calculations of VLF motions at this site [*MacMahan et al.*, 2004; *Reniers et al.*, 2007]. Model predictions of the resulting Eulerian VLF velocity response at ADCP5 are comparable to the observations with similar timescales and intensity in the cross-shore velocity (Figure 9). Vertical variation in the VLF velocities is relatively weak in both the model and observations. Note that the correspondence is not expected to be deterministic given the stochastic wave group forcing obtained from the frequency-directional incident spectra [*Reniers et al.*, 2007].

[20] The intensity of the VLF motions is defined by the RMS VLF speed, $U_{rms,vlf}$:

$$U_{rms,vlf} = \sqrt{\int_{\delta f}^{0.004Hz} S_{uu}(f) + S_{vv}(f)df} \qquad (8)$$

where the frequency resolution, δf, equals 0.000278 Hz and $S_{uu}(f)$ and $S_{vv}(f)$ represent the variance density spectra of the cross-shore and alongshore velocities based on 3 h long time series. This definition holds for both measurements and model computations.

[21] Comparing the calculated and observed RMS VLF velocities at ADCP5 for the 3 day duration shows that 76% of the observed variability is explained (Table 1). Similar results are obtained at the other ADCPs, explaining 55% and 81% of the variability at ADCP4 and ADCP6, respectively. The skill for the PDEM sensors located within the surf zone, evaluated near the bed, show similar performance (Table 1) which is consistent with previous model efforts at this site explaining O(60)% of the observed VLF velocity

variability [*Reniers et al.*, 2007]. This suggests that the model successfully predicts the VLF motions.

[22] This concludes the model verification for the wave transformation, mean Eulerian and Lagrangian surface flows and concurrent VLF motions. The next step is to examine the retention of surface floating material.

8. Surf Zone Exits

[23] In each hourly computation for yeardays 124 through 126, the surf zone area extending approximately 50 m from the shore line (consistent with the field drifter deployments (MacMahan et al., submitted manuscript, 2009)), is seeded with an initially uniform distribution of drifters at 10 m spacing (Figure 10). Drifter trajectories are then calculated at each 3 s time step on the basis of the instantaneous velocity field with subgrid accuracy. Using the GLM velocities to compute the trajectories results in persistent circular paths with the occasional drifter exiting the surf zone (Figure 10 (left)). The outer edge of the surf zone is

Table 1. RMS-VLF Model Skill for the 3 Day Duration From Yeardays 124–127

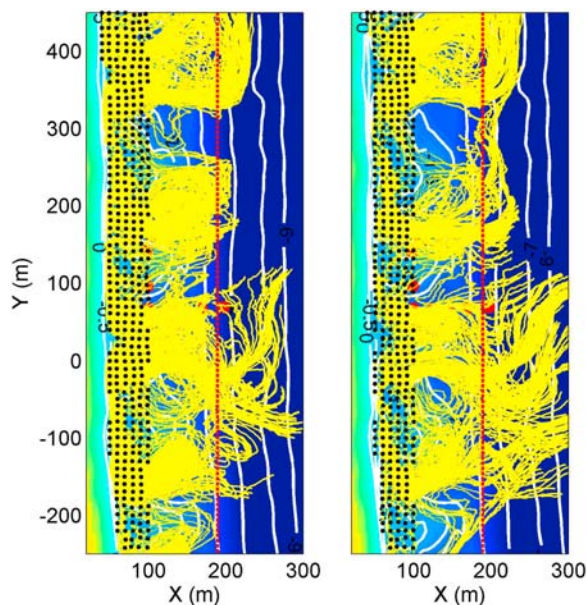| Sensor	Model Skill
PDEM1	0.62
PDEM2	0.43
ADCP4	0.55
ADCP5	0.76
ADCP6	0.81
PDEM7	0.78
PDEM8	0.75
PDEM9	0.60
PDEM10	0.49
PDEM11	0.74

Figure 10. Initial drifter locations (black circles) and calculated trajectories (yellow dots) for yearday 124 h 10.00 using (left) GLM velocities and (right) Eulerian velocities. Position of the outer surf zone edge indicated by red dashed line. Bathymetry with depth contours in meters given as a reference. Instrument locations indicated by red dots.

defined as the location where the alongshore-averaged cross-shore roller energy, a proxy for wave breaking induced intensity [*Aarninkhof*, 2003], exceeds 10% of its cross-shore maximum (Figure 10). Note that a significant number of drifters that do exit the surf zone re-enter at a later time. In contrast, using the Eulerian velocity to calculate the drifter trajectories results in a significant increase in the number of drifter exits and re-entry of drifters is sporadic (Figure 10 (right)). At the end of the hour the number of drifters that have exited the surf zone within the interior domain, $-250\ m < Y < 450\ m$, is collected and expressed as a percentage of the total number of active drifters initially present during that hour.

[24] Next, the hourly results over the 3 day period from yearday 124 through 126 are analyzed. The computed percentage of drifter exits were related to a number of physical variables, including tidal elevation, offshore wave height, wave period, depth at breaking, mass flux, etc. The optimal correlation is obtained with what is defined as the exit parameter:

$$E = \frac{X_w}{H_{rms,o} T_{m01}} \qquad (9)$$

with the surf zone width, X_w, the RMS wave height at the offshore boundary, $H_{rms,o}$, and T_{m01} as the mean wave period (Figure 11). The observed drifter exits obtained from the GPS drifters on days of near normal wave incidence, where X_w is obtained from video time exposures (MacMahan et al., submitted manuscript, 2009), support the computational results. The number of GLM-calculated drifter exits increases for increasing surf zone width and decreasing wave height (Figure 11), indicating a relation

between the beach slope and drifter exits, which suggests more drifter exits for dissipative beaches (mild slope) compared with reflective beaches (steeper slope). The linear correlation coefficient, r, for $X_w/H_{rms,o}$ is 0.65 with a 95% confidence interval of (0.54, 0.80). The inclusion of the wave period accounts for shoaling and wave steepness effects thereby increasing the correlation to r = 0.75 with a 95% confidence interval of (0.62,0.84) (Figure 11). Note that the present results are not only a function of the hydrodynamics, as expressed by the drifter exit parameter E, but also the underlying rip-channeled bathymetry. Hence the general validity of the exit parameter still needs to be established.

[25] Using the Eulerian velocities to calculate the drifter trajectories, typically 80% of the active drifters exit the surf zone within the hour (Figure 11). This percentage of drifter exits is almost an order of magnitude larger than the observed $O(20)$% exits. The large difference between the calculated Eulerian and GLM drifter exits and the fact that the latter are much closer to the observations strongly supports the inclusion of the Stokes drift to calculate the fate of floating surf zone material. This result seems surprising at first given the fact that the velocity differences for the GLM and Eulerian flow patterns are relatively small (Figure 4). However, the net transport direction is a delicate balance between the onshore-directed Stokes drift and offshore-directed Eulerian velocities at the outer surf zone. The fact that Stokes drift reduces the offshore Eulerian velocity, thus increasing the relative importance of the
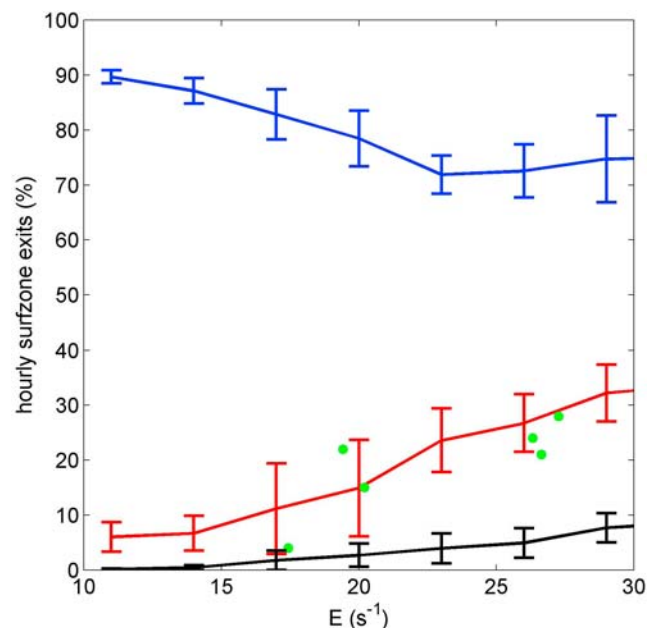

Figure 11. Model-estimated percentage of the hourly exits versus the drifter exit parameter E. Exits calculated with GLM (solid red line), Eulerian (solid blue line), and hourly mean (without VLFs) (solid black line) velocities ±1 standard deviation (denoted by the vertical bars) for yeardays 124 through 126. Observations of percentage drifter exits indicated by green dots on yeardays 117, 124, 125, 127, 130, and 135 corresponding to times of normally incident waves during RCEX.

alongshore velocities, results in a stronger lateral transport of the drifters to the outer edge of the shoal (Figure 5 (left)). At this location the GLM velocities generally have a small net onshore velocity (Figure 5 (right)) pushing the drifters back thereby retaining the majority of the surface drifters (Figure 10 (left)). In contrast, without Stokes drift there is little time for the drifters to travel sideways, thus rarely reaching an area with onshore flow (Figure 5 (middle)), resulting in a near complete exit of the drifters within 1 h (Figure 11).

[26] The GLM velocity snapshot (Figure 3) suggests that VLFs may be important in transporting surface flow material offshore. To assess the effect of excluding the VLF motions on the drifter trajectories, the VLF motions are filtered out by applying an hourly running mean on the computed GLM velocities. In that case, almost all of the drifters are retained within the surf zone corresponding to an hourly exit percentage of less than 5% (Figure 11), which is significantly less that the observed exit percentages. These results suggest that the VLF motions are indeed an important factor in the exchange of surface floating material between the surf zone and inner shelf and should be included in modeling their fate within the nearshore.

9. Conclusions

[27] A 3-D wave and flow model was used to compute the wave and velocity field at the wave group timescale. Comparison with in situ ADCP measurements show that the hourly mean velocity variation is qualitatively well represented. Important differences do occur, most notably in the prediction of the vertical structure of the rip current flow at the outer surf zone, where the observed strong vertical attenuation is not present in the computations and the intensity of the alongshore current is under predicted. Model predictions typically explain 60% of the VLF variance at both ADCPs (near-surface flows) and PDEMs (near bed flows). The GPS drifter-inferred velocity patterns are also well predicted in both velocity magnitude and orientation (skill of $O(0.6)$).

[28] The calculated surface velocity fields, at the wave group timescale, are used to predict the trajectories of virtual surface drifters. This is done for GLM velocities (including Stokes drift) and Eulerian velocities (without Stokes drift). The latter generally results in a near complete exodus of the drifters within the hour. A detailed examination of the computed flow velocities at the outer surf zone shows that the mean Eulerian flow field generally has smaller onshore velocities and stronger offshore-directed velocities, occasionally resulting in predicted flows moving in opposite directions when the Stokes drift dominates the offshore-directed Eulerian flow. The majority of the GLM calculated drifter velocities are still within the surf zone after 1 h. This is a result of the fact that the GLM velocities include the Stokes drift, which reduces the offshore flows allowing more rotation at the outer edge of the surf zone (Figure 5). The GLM derived results are consistent with the field observations, whereas the Eulerian results overpredict the number of drifter exits by almost an order of magnitude. This stresses the importance of including Stokes drift in calculating the transport of surface floating material. In addition, model calculation with the VLF motions averaged

out of the GLM velocity field result in fewer than 5% hourly drifter exits, i.e., significantly less than the observations, suggesting that the VLF motions are also important in the transport of surface floating material. Only the combination of Stokes drift and VLF motions results in drifter exit percentages comparable to the observations of $O(20)$%.

[29] The resulting hourly retention rates, based on the fraction of drifters retained in the surf zone within 1 h, are 80% for the GLM velocities and 20% for the Eulerian velocities. Assuming retention decays exponentially with time this results in a relaxation timescale of $O(5)$ h for the GLM velocities and less than 1 h for the Eulerian velocities. As a result, the retention time of floating surf zone material on a rip-channeled beach can be significantly longer than originally anticipated. This likely also holds for other suspended material such as sediment fines, algae, bubbles, larvae, and other organic matter that track the fluid motions and are therefore subject to Stokes drift. However, their retention also depends on the vertical advection given the fact these agents are not necessarily confined to the water surface only and the GLM velocities vary with depth.

Appendix A

[30] The wave and flow computations operate on the wave group timescale. To that end, the measured hourly frequency-directional wave spectra at 13 m water depth are used to generate a time series of wave energy at the offshore boundary using the method outlined by *van Dongeren et al.* [2003]. The wave energy is subsequently propagated in the model domain with the wave energy balance:

$$\frac{\partial E_w}{\partial t} + \frac{\partial E_w c_g \cos(\theta)}{\partial x} + \frac{\partial E_w c_g \sin(\theta)}{\partial y} = -D_w \quad (A1)$$

where E_w represents the wave energy, D_w is the dissipation of wave energy due to breaking modeled with the dissipation formulation of *Roelvink* [1993], and x, y are the cross-shore (positive onshore) and alongshore coordinates following the Cartesian convention. The wave direction, θ, has been obtained from a SWAN computation (Figure A1). The local phase, c, and group, c_g, speeds within the model domain are calculated with linear wave theory using the mean wave period, T_{m01}, also obtained from the SWAN calculation (Figure A1). Wave energy dissipation due to wave breaking acts as a source term in the roller energy balance [*Nairn et al.*, 1990; *Stive and de Vriend*, 1994]:

$$\frac{\partial E_r}{\partial t} + \frac{\partial 2E_r c \cos(\theta)}{\partial x} + \frac{\partial 2E_r c \sin(\theta)}{\partial y} = D_w - D_r \quad (A2)$$

where D_r represents the roller energy dissipation. The roller-related Stokes drift is calculated with [*Svendsen*, 1984]:

$$\mathbf{u^r} = \frac{2E_r}{\rho c h} \frac{\mathbf{k_w}}{k_w} \quad (A3)$$

and $\mathbf{k_w}$ represents the wave number vector of the incident waves with magnitude k_w.
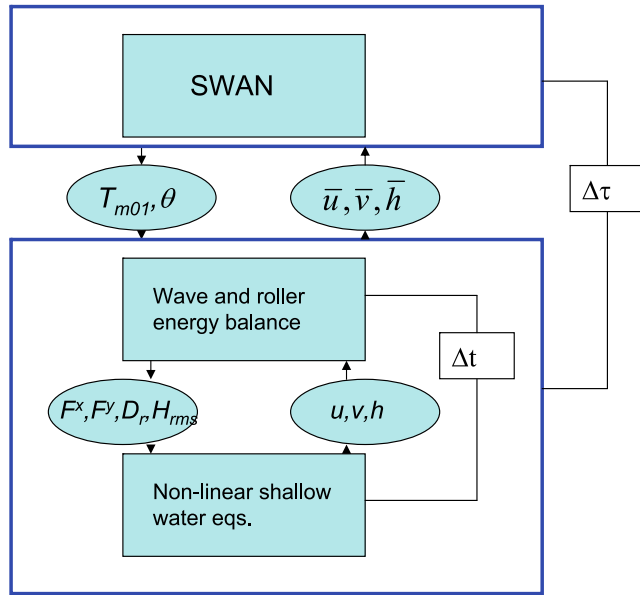
Figure A1. Flow diagram for hydrodynamic computations.

[31] Wave and roller energy are used to calculate the radiation stresses using linear wave theory and the roller energy dissipation is used to calculate the shear stress at the surface [*Dingemans et al.*, 1987; *Deigaard*, 1993]:

$$\boldsymbol{\tau}_s = \frac{D_R}{c}\frac{\mathbf{k_w}}{k_w} \qquad (A4)$$

The total wave forcing is given by the radiation stress gradients (including the roller contribution [*Reniers et al.*, 2004]):

$$F^x = \frac{1}{\rho h}\left(\frac{\partial S_{xx}}{\partial x} + \frac{\partial S_{xy}}{\partial y}\right)$$
$$F^y = \frac{1}{\rho h}\left(\frac{\partial S_{yx}}{\partial x} + \frac{\partial S_{yy}}{\partial y}\right) \qquad (A5)$$

and subtracting the wave breaking related surface shear stress from the total wave forcing yields the (irrotational) body force:

$$F_B^x = \frac{1}{\rho h}\left(\frac{\partial S_{xx}}{\partial x} + \frac{\partial S_{xy}}{\partial y}\right) - \tau_s^x$$
$$F_B^y = \frac{1}{\rho h}\left(\frac{\partial S_{yx}}{\partial x} + \frac{\partial S_{yy}}{\partial y}\right) - \tau_s^y \qquad (A6)$$

which is applied as a depth invariant forcing term in the nonlinear shallow water momentum balance (equation (4)). Next the 3-D flow response is calculated as outlined by *Lesser et al.* [2004]. Both wave and roller energy balances and the nonlinear shallow water equations are numerically solved with finite difference equations with a time step Δt of 3 s. After 5 min, corresponding to $\Delta \tau$, a new SWAN computation is performed which includes the effects of the slowly varying current on the calculations of the mean

period and the mean wave angle by using a 5 min average of the depth-averaged GLM velocity field obtained from the flow computations (denoted by overbarred quantities in Figure A1). The 5 min averaging eliminates most of the infragravity motions but still resolves the VLF motions. Using a 2 min $\Delta \tau$ interval and averaging resulted in negligible differences in computed mean and VLF motions.

References

Aarninkhof, S. G. J. (2003), Nearshore bathymetry derived from video imagery, Ph.D. thesis, 175 pp., Delft Univ. of Technol., Delft, Netherlands.
Andrews, D. G., and M. E. McIntyre (1978), An exact theory of non-linear waves on a Lagrangian-mean flow, *J. Fluid Mech.*, *98*, 609–646.
Battjes, J. A. (1975), Modeling of turbulence in the surf zone, in *Symposium on Modeling Techniques: 2d annual symposium of the Waterways, Harbors, and Coastal Engineering Division of ASCE, San Francisco, California, September 3–5, 1975*, pp. 1050–1061, Am. Soc. of Civ. Eng., New York.
Booij, N., R. C. Ris, and L. H. Holthuijsen (1999), A third generation model for coastal regions, Part I: Model description and validation, *J. Geophys. Res.*, *104*, 7649–7666.
Brown, J. W., J. H. MacMahan, A. J. H. M. Reniers, and E. B. Thornton (2008), Surfzone diffusivity on a rip channeled beach, *J. Geophys. Res.*, doi:10.1029/2008JC005158, in press.
Clarke, L. B., D. Ackerman, and J. Largier (2007), Dye dispersion in the surfzone: Measurements and simple models, *Cont. Shelf Res.*, *27*, 650–669.
Deigaard, R. (1993), A note on the three dimensional shear stress distribution in a surf zone, *Coastal Eng.*, *20*, 157–171.
Dingemans, M. W., A. C. Radder, and H. J. de Vriend (1987), Computation of the driving forces of wave-induced currents, *Coastal Eng.*, *11*, 539–563.
Dodd, N., V. Iranzo, and A. J. H. M. Reniers (2000), Shear instabilities of wave-driven alongshore currents, *Rev. Geophys.*, *38*, 437–463.
Feddersen, F. (2007), Breaking wave induced cross-shore tracer dispersion in the surf one: Model results and scalings, *J. Geophys. Res.*, *112*, C09012, doi:10.1029/2006JC004006.
Gallagher, E. L., S. Elgar, and R. T. Guza (1998), Observations of sand bar evolution on a natural beach, *J. Geophys. Res.*, *103*, 3203–3215.
Grant, S., J. H. Kim, B. H. Jones, S. A. Jenkins, J. Wasyl, and C. Cudaback (2005), Surfzone entrainment, longshore transport and human health implications of pollution from tidal outlets, *J. Geophys. Res.*, *110*, C10025, doi:10.1029/2004JC002401.
Groeneweg, J., and G. Klopman (1998), Changes of the mean velocity profiles in the combined wave-current motion in a GLM formulation, *J. Fluid Mech.*, *370*, 271–296.

Haas, K. A., and J. C. Warner (2009), Comparing a quasi-3D to a full 3D nearshore circulation model: SHORECIRC and ROMS, *Ocean Modell.*, *26*, 91–103, doi:10.1016/j.ocemod.2008.09.003.

Haas, K. A., I. A. Svendsen, M. C. Haller, and G. Zhao (2003), Quasi-three-dimensional modeling of rip current system, *J. Geophys. Res.*, *108*(C7), 3217, doi:10.1029/2002JC001355.

Haller, M. C., and D. A. Dalrymple (2001), Rip current instabilities, *J. Fluid Mech.*, *433*, 161–192.

Inman, D. L., and B. M. Brush (1973), The coastal challenge, *Science*, *181*, 20–32.

Inman, D. L., F. J. Tait, and C. E. Nordstrom (1971), Mixing in the surfzone, *J. Geophys. Res.*, *76*, 3493–3514.

Johnson, D., and C. Pattiaratchi (2004), Application, modeling and validation of surfzone drifters, *Coastal Eng.*, *51*, 455–471.

Komar, P. D. (1976), *Beach Processes and Sedimentation*, 429 pp., Prentice-Hall, Englewood Cliffs, N. J.

Lesser, G. R., J. A. Roelvink, J. A. T. M. van Kester, and G. S. Stelling (2004), Validation and development of a three-dimensional morphological model, *Coastal Eng.*, *51*, 883–915.

MacMahan, J. H. (2001), Hydrographic surveying from a personal watercraft, *J. Surv. Eng.*, *127*, 12–24.

MacMahan, J. H., A. J. H. M. Reniers, E. B. Thornton, and T. P. Stanton (2004), Surf zone eddies coupled with rip current morphology, *J. Geophys. Res.*, *109*, C07004, doi:10.1029/2003JC002083.

MacMahan, J. H., T. P. Stanton, E. B. Thornton, and A. J. H. M. Reniers (2005), RIPEX: Observations of a rip current system, *Mar. Geol.*, *218*, 113–134.

MacMahan, J., J. Brown, and E. B. Thornton (2008), Low-cost handheld Global Positioning Systems for measuring surf zone currents, *J. Coastal Res.*, *25*, 744–754, doi:10.2112/08-1000.1.

Mellor, G. L. (2003), The three-dimensional current and surface wave equations, *J. Phys. Oceanogr.*, *33*, 1978–1989.

Monismith, S. G., and D. A. Fong (2004), A note on the transport of scalars and organisms by surface waves, *Limnol. Oceangr.*, *49*, 1214–1219.

Nairn, R. B., J. A. Roelvink, and H. N. Southgate (1990), Transition zone width and implications for modeling surfzone hydrodynamics, in *Coastal Engineering (1990)*, edited by B. L. Edge, pp. 68–81, Am. Soc. Civ. Eng., New York.

Nobuoka, H., N. Mimura, and J. A. Roelvink (2004), Three-dimensional nearshore currents model using sigma coordinate system, in *Coastal Engineering 2004*, vol. 1, edited by J. McKee Smith, pp. 1429–1441.

Özkan-Haller, H. T., and J. T. Kirby (1999), Nonlinear evolution of shear instabilities of the longshore current: A comparison of observations and computations, *J. Geophys. Res.*, *104*, 25,953–25,984.

Phillips, O. M. (1977), *The Dynamics of the Upper Ocean*, Cambridge Univ. Press, Cambridge, U. K.

Plant, N. G., K. L. Edwards, J. M. Kaihatu, J. Veeramony, L. Hsu, and T. Holland (2009), The effect of bathymtric filtering on nearshore process model results, *Coastal Eng.*, *56*, 484–493.

Putrevu, U., and I. A. Svendsen (1999), Three-dimensional dispersion of momentum in wave-induced nearshore currents, *Eur. J. Mech. B*, *18*, 409–427.

Reniers, A. J. H. M., J. A. Roelvink, and E. B. Thornton (2004), Morphodynamic modeling of an embayed beach under wave group forcing, *J. Geophys. Res.*, *109*, C01030, doi:10.1029/2002JC001586.

Reniers, A. J. H. M., J. MacMahan, E. B. Thornton, and T. Stanton (2006), Modeling infragravity motions on a rip-channel beach, *Coastal Eng.*, *53*, 209–222.

Reniers, A., J. MacMahan, E. B. Thornton, and T. P. Stanton (2007), Modeling of very low frequency motions during RIPEX, *J. Geophys. Res.*, *112*, C07013, doi:10.1029/2005JC003122.

Roelvink, J. A. (1993), Dissipation in random wave groups incident on a beach, *Coastal Eng.*, *19*, 127–150.

Roelvink, J. A., and M. J. F. Stive (1989), Bar generating cross-shore flow mechanisms on a beach, *J. Geophys. Res.*, *94*, 4785–4800.

Spydell, M., F. Feddersen, R. Guza, and W. Schmidt (2007), Observing surfzone dispersion with drifters, *J. Phys. Oceanogr.*, *37*, 2920–2939.

Stive, M. J. F., and H. J. de Vriend (1994), Shear stresses and mean flow in shoaling and breaking waves, in *Coastal Engineering (1994)*, edited by B. L. Edge, pp. 594–608, Am. Soc. of Civ. Eng., New York.

Stokes, C. G. (1847), On the theory of oscillatory waves, *Trans. Cambridge Philos. Soc.*, *8*, 441–455.

Svendsen, I. A. (1984), Mass flux and undertow in a surf zone, *Coastal Eng.*, *8*, 347–365.

van Dongeren, A. R., A. J. H. M. Reniers, J. A. Battjes, and I. A. Svendsen (2003), Numerical modelling of infragravity wave response during Delilah, *J. Geophys. Res.*, *108*(C9), 3288, doi:10.1029/2002JC001332.

Walstra, D. J. R., J. A. Roelvink, and J. Groeneweg (2000), Calculation of wave-driven currents in a mean flow model, in *Coastal Engineering (2000)*, edited by B. L. Edge, pp. 1050–1063, Am. Soc. of Civ. Eng., Reston, Va.

————————————

J. A. Brown, J. H. MacMahan, T. P. Stanton, and E. B. Thornton, Department of Oceanography, Naval Postgraduate School, Monterey, CA 93943, USA.

J. W. Brown, Center for Applied Coastal Research, University of Delaware, Newark, DE 19716, USA.

E. Gallagher, Department of Biology, Franklin and Marshall College, Lancaster, PA 17604–3003, USA.

M. Henriquez, Department of Hydraulic Engineering, Delft University of Technology, NL-2600 AA Delft, Netherlands.

A. J. H. M. Reniers, Applied Marine Physics Department, Rosenstiel School of Marine and Atmospheric Science, University of Miami, Miami, FL 33149, USA. (areniers@rsmas.miami.edu)